

Research Article

Influence of the Mesoscopic Viscoelastic Contact Model on Characterizing the Rheological Behavior of Asphalt Concrete in the DEM Simulation

Jiaolong Ren ¹, Zhe Liu,² Jinshun Xue ³, and Yinshan Xu⁴

¹School of Civil and Architectural Engineering, Shandong University of Technology, Zibo 255000, China

²Zhejiang Provincial Institute of Communications Planning, Design & Research, Hangzhou 310031, China

³School of Civil Engineering and Architecture, Hubei University of Arts and Science, Xiangyang 441053, China

⁴Zhejiang Scientific Research Institute of Transport, Hangzhou 310039, China

Correspondence should be addressed to Jiaolong Ren; worjl@126.com and Jinshun Xue; jinshunx@chd.edu.cn

Received 2 December 2019; Accepted 17 January 2020; Published 8 February 2020

Academic Editor: Damien Rangaard

Copyright © 2020 Jiaolong Ren et al. This is an open access article distributed under the Creative Commons Attribution License, which permits unrestricted use, distribution, and reproduction in any medium, provided the original work is properly cited.

The numerical simulation based on the discrete element method (DEM) is popular to analyze the material behavior of asphalt concrete in recent years because of the advantage of the DEM in characterizing the heterogeneous microstructures. As a type of viscoelastic material, the rheological behavior of asphalt concrete is represented depending on the mesoscopic viscoelastic contact model between two particles in a contact in DEM simulations. However, what is missing in the existing literature studies is analysis of the influence of the mesoscopic viscoelastic contact models. Hence, the existing mesoscopic viscoelastic contact models are employed to build different types of DEM numerical samples of asphalt concrete in this study. Laboratory tests and the corresponding numerical tests at different temperatures and frequencies are implemented to investigate the difference in simulation precision in the case of using different mesoscopic viscoelastic contact models via the rheological index of dynamic modulus and phase angle. The results show the following: (1) the mesoscopic generalized Maxwell contact model provides the best simulation precision at low temperatures; (2) the mesoscopic generalized Kelvin contact model shows an improved precision at high temperatures; and (3) although the mesoscopic Burgers contact model has the simplest mathematical structure, the simulation precisions are obviously lower than those of the other two contact models, particularly when simulating the phase angle at low temperatures and frequencies. The results will be beneficial to select the appropriate mesoscopic contact model for the DEM modeling of asphalt concrete according to the loading conditions.

1. Introduction

Asphalt concrete is one of the most important construction materials in the highway industry [1], which can be treated as a three-level distributed system: the coarse aggregates, the asphalt mastics, and the voids [2, 3]. The existence of coarse aggregates leads to the conspicuous granular behavior of asphalt concrete [4, 5]. Hence, the discrete element method (DEM) introduced by Cundall and Strack [6, 7] for studying granular materials [8] draws engineers' great attention. Since the mid-2000s, the DEM has become a prevailing modeling and simulation method for studying the performance of asphalt concrete, of which the foremost advantage for

characterizing some important mechanical and structural performance of asphalt concrete is that the method provides an explicit treatment of the materials at a mesoscopic level.

In the numerical simulation based on the DEM, asphalt concrete is always modeled using three parts: the coarse aggregate elements, the asphalt mastic elements, and the void elements. The performance of the aggregate-mastic interaction is characterized as that of contacts between coarse aggregate elements and asphalt mastic elements. Materials in the DEM are modeled as a system of distinct, interacting, and spherical particles subject to motion and deformation. A force-displacement law updated each time step is acted on the contacts between particles, from which

macroscopic characteristics of materials are obtained through the interaction of contacts between particles at the mesoscopic scale. Thereupon, complex mechanical characteristics of materials can be elucidated by DEM simulations [9]. The focus of this paper is the force-displacement law (i.e., the mesoscopic contact model) in the DEM.

In the DEM models, the coarse aggregates treated as the densely assembled elastic particles described their interactions by the mesoscopic elastic contact models. The asphalt mastics, containing the asphalt binder, fine aggregates, and mineral powder, are treated as the densely assembled viscoelastic particles with equal radius, and their interactions are described through the mesoscopic viscoelastic contact models. Obviously, the mesoscopic viscoelastic contact models acting on the interactions of asphalt mastic particles play a significant role in characterizing the rheological behavior of asphalt concrete.

In the past decade, the applied mesoscopic viscoelastic contact models are increasingly complex. At first, the simple bond contact model was used to describe the viscoelastic properties of asphalt mastics in the studies of Kim et al. [10–12] and Mahmoud et al. [13]. Afterwards, Qian et al. [14] and Yang et al. [15] adopted the cohesive models to reflex the viscosity characteristics of asphalt mastics. Meanwhile, a mesoscopic Burgers viscoelastic contact model (embedded by “Itasca Corporation”) instead of the simple bond contact models was applied in analyzing the viscoelastic mechanical response of asphalt concrete [16–34]. Research showed that mesoscopic viscoelastic contact models influenced the asphalt concrete performance significantly, especially the rheological behavior. The Burgers contact models used in these studies are all invoked directly from the software (PFC) produced by Itasca Corporation. Subsequently, Ren and Sun [35] developed a new mesoscopic viscoelastic contact model, namely, the mesoscopic generalized Maxwell contact model, which could describe the low-temperature rheological behavior of asphalt concrete more accurately than the mesoscopic Burgers contact model in the DEM [36–38]. Shimizu et al. [39] and Jin et al. [40] put forward the mesoscopic generalized Kelvin contact model in the DEM but had not been applied to asphalt-based materials.

The mesoscopic Burgers contact model (B-model), the mesoscopic generalized Maxwell contact model (M-model), and the mesoscopic generalized Kelvin contact model (K-model) are the only three mesoscopic viscoelastic contact models in the DEM simulations at present. However, what is missing in the existing literature studies is analysis of the influence of the three mesoscopic viscoelastic contact models on characterizing the rheological behavior of asphalt concrete. Hence, there is not efficient guidance that selects the appropriate mesoscopic viscoelastic contact model under different loading conditions in the DEM simulations.

In response to the above problem, three types of asphalt concrete DEM models using the B-model, M-model, and K-model are built to investigate the difference in their rheological behaviors compared to the experimental data based on the dynamic modulus and phase angle via the dynamic modulus tests in the case of different temperatures (−6°C, 4°C, 16°C, 27°C, and 38°C) and loading frequencies

(0.1 Hz, 0.5 Hz, 1 Hz, 5 Hz, 10 Hz, and 25 Hz). The results will be beneficial to select the appropriate mesoscopic contact model for the DEM modeling of asphalt concrete according to the loading conditions.

2. DEM Model of Asphalt Concrete

2.1. Numerical Sample. Figure 1 shows the numerical sample of asphalt concrete using a 2D DEM modeling technology proposed in our previous study [36] based on the software PFC. The numerical sample contained coarse aggregate elements (red region), asphalt mastic elements (black region), and void elements (white region).

The coarse aggregate elements represent the aggregates whose diameters are larger than 1.18 mm. The asphalt mastic elements represent the combination of the asphalt binder and fine aggregates whose diameters are smaller than 1.18 mm. The coarse aggregate elements and asphalt mastic elements are both treated as densely assembled balls with an equal radius (0.5 mm), and there is no ball in the void elements.

2.2. Constitutive Relations of Different Contacts in Numerical Samples. In the numerical sample, four types of contacts in the numerical sample of asphalt concrete are used to represent four different interactions: contacts within coarse aggregate elements, between adjacent coarse aggregate elements, between coarse aggregate elements and asphalt mastic elements, and within asphalt mastic elements. Obviously, the properties of any contact in the numerical samples can be characterized through getting the corresponding mesoscopic contact models of the two balls (two identical aggregate elements, two different aggregate elements, two identical mastic elements, or one aggregate element and a mastic element) in a contact.

Figures 2–4 present the constitutive relations of different contacts in the numerical samples using the B-model, M-model, and K-model, respectively. Thereinto, k and η represent the spring stiffness and the Newton dashpot viscosity. The superscripts a and b represent the parameters of the two balls in contact. The superscripts B , M , and K represent the values of physical quantities in the case of using the B-model, the M-model, and the K-model. The subscripts n and s represent the values of physical quantities in the normal direction and shear direction.

As shown in Figures 2–4, the constitutive relations within aggregates and between adjacent aggregates are the same among different types of numerical samples, which are described via two tandem springs acting on the coarse aggregate element.

The constitutive relations between aggregates and asphalt mastics are characterized via stringing one spring acting on the coarse aggregate element and one mesoscopic viscoelastic contact model acting on the asphalt mastic element. The constitutive relations within asphalt mastics are represented via two tandem mesoscopic viscoelastic contact models acting on the asphalt mastic element.

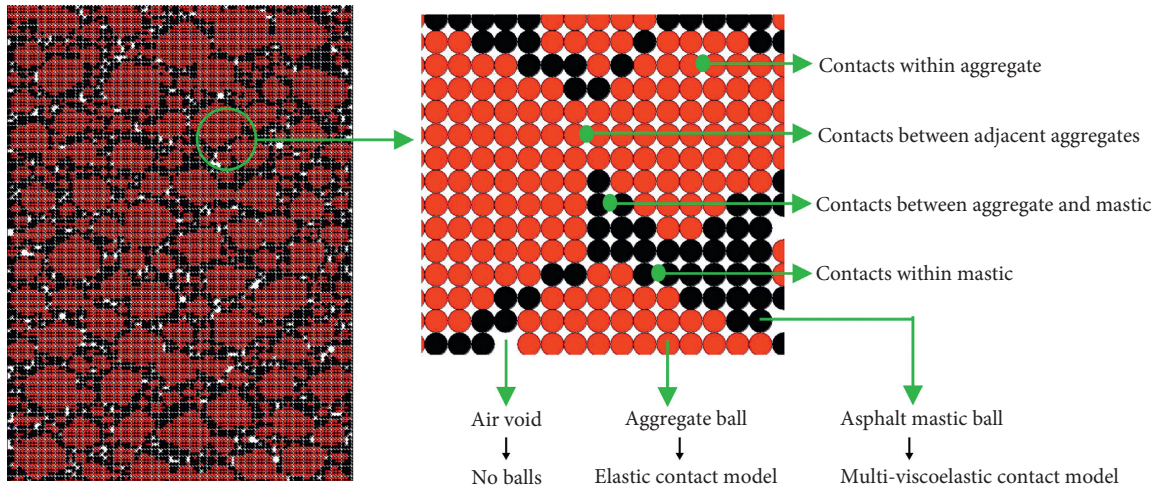


FIGURE 1: Numerical sample of asphalt concrete.

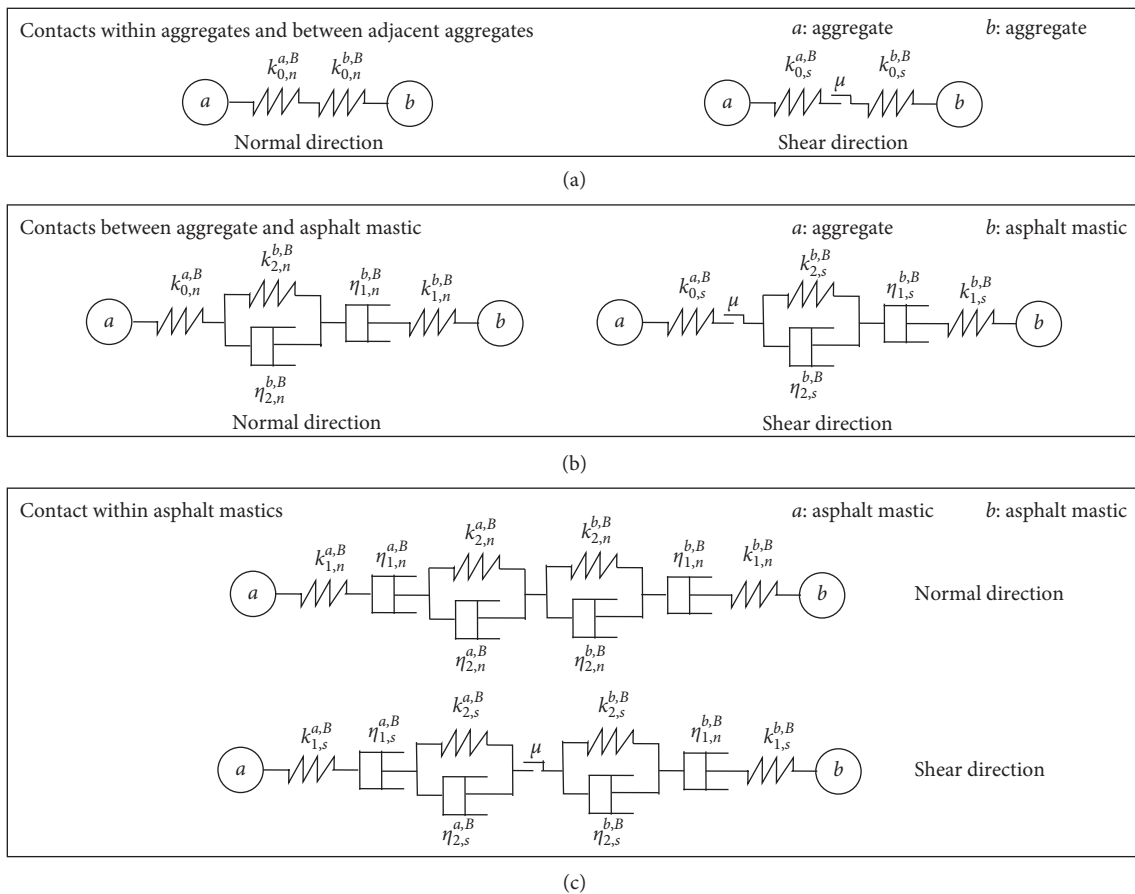


FIGURE 2: Constitutive relation of contacts in numerical samples using the B-model.

As previously mentioned, the B-model is employed as the built-in model of PFC in the existing studies. The M-model and the K-model have been developed by Ren and Sun [35] and Shimizu et al. [39] via the finite difference time-domain method [41], respectively. For a more detailed and rigorous introduction about the mathematic relations of the M-model and K-model, readers can refer to the studies of Ren and Sun [35] and Shimizu et al. [39].

2.3. *Parameter Calibration of Constitutive Relations.* The parameters of the constitutive relations shown in Figures 2–4 can be estimated indirectly using the inference from parameters of the corresponding macroscopic constitutive models. The parameters of the springs are obtained via the Young modulus of the coarse aggregates in the existing studies. The parameters of the mesoscopic viscoelastic contact models are usually calculated via the dynamic

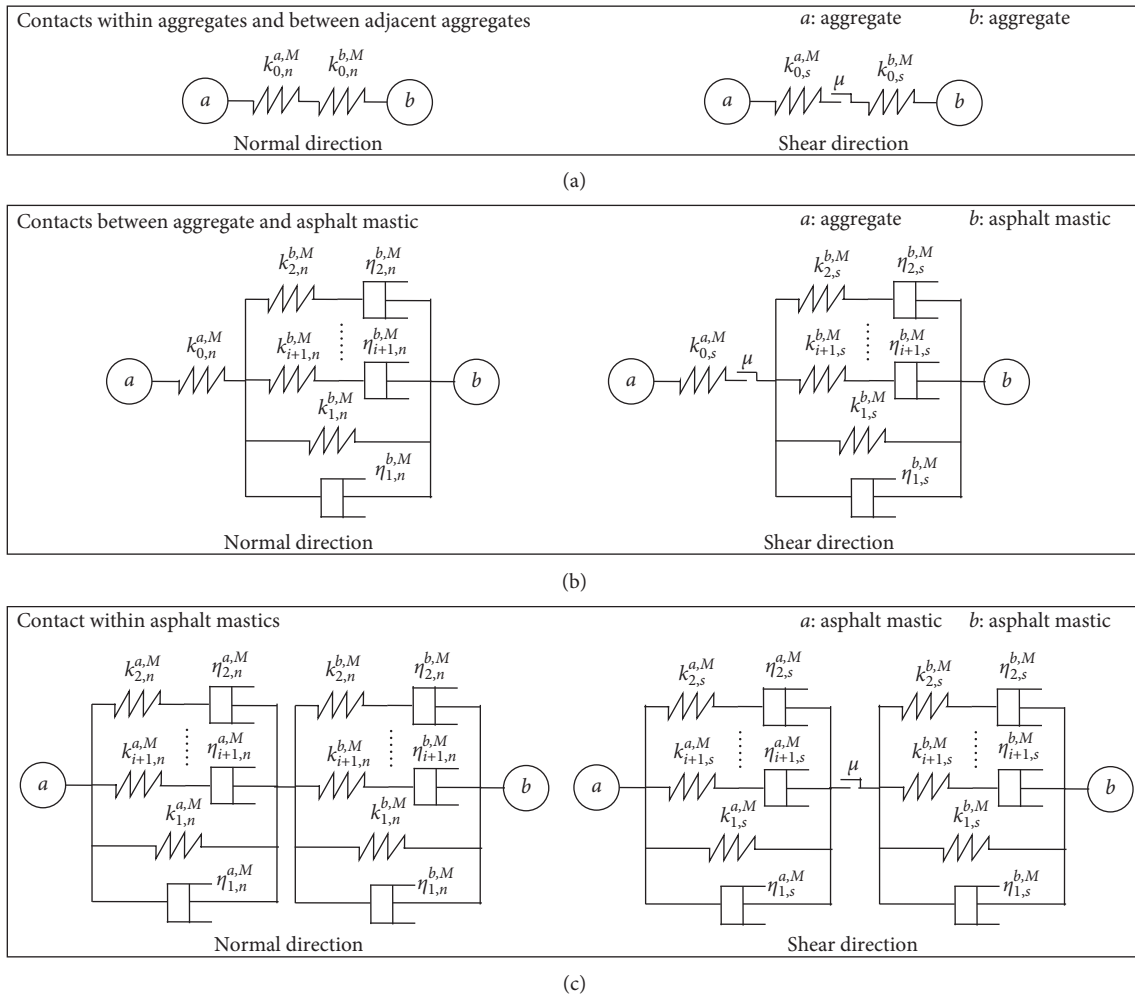


FIGURE 3: Constitutive relation of contacts in numerical samples using the M-model.

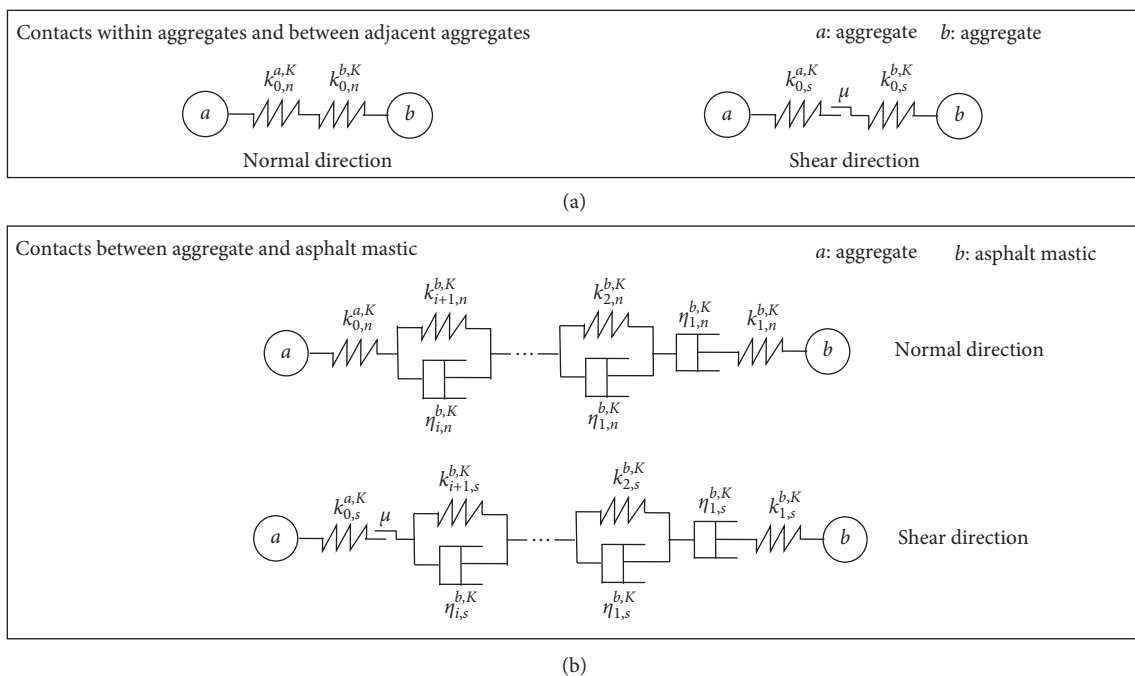


FIGURE 4: Continued.

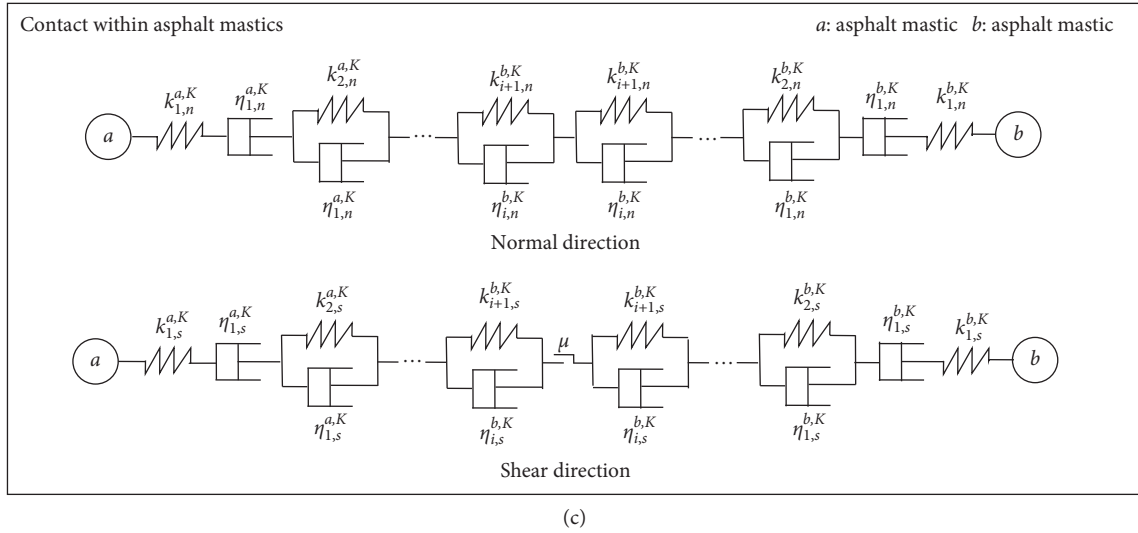


FIGURE 4: Constitutive relation of contacts in numerical samples using the K-model.

modulus and phase angle of the asphalt mastic at different frequencies. The parameter calibration method of the B-model, the M-model, and the K-model has been established by Liu and You [22], Ren and Sun [35], and Jin et al. [40], respectively, which is not detailedly introduced here.

The Young modulus of the coarse aggregates is 59.2 GPa. The gradation of the asphalt mastic used in this study is shown in Table 1.

The dynamic modulus and phase angle of the asphalt mastic are measured at different temperatures (-6°C , 4°C , 15°C , 27°C , and 38°C) and frequencies (0.1 Hz, 0.5 Hz, 1 Hz, 5 Hz, 10 Hz, and 25 Hz), of which the testing results are shown in Figure 5. The parameters of the numerical samples using the B-model, the M-model, and the K-model are listed in Tables 2–4, respectively.

The parameters can be assigned to the discrete elements using the PFC command “prop pa_name pa_value range id id_DE.” “prop,” “range,” and “id” are the built-in commands of PFC. “pa_name” and “pa_value” are the name and the value of the target parameter. “id_DE” is the ID number of the discrete element.

3. Laboratory Tests and Numerical Tests

3.1. Laboratory Tests. The material composition of asphalt concrete used in this study is listed in Table 5.

The dynamic modulus tests of asphalt concrete are carried out at the temperatures of -6°C , 4°C , 16°C , 27°C , and 38°C and at the frequencies of 0.1 Hz, 0.5 Hz, 1 Hz, 5 Hz, 10 Hz, and 25 Hz, of which the result data are shown in Figure 6. The dynamic modulus-testing apparatus is shown in Figure 7. All the laboratory tests are implemented according to the Chinese testing specification “Standard Test Methods of Bitumen and Bituminous Mixtures for Highway Engineering (JTG E20-2011),” and four samples were tested successfully in each testing condition.

The following preparation method (Figure 8) of asphalt concrete samples and asphalt mastic samples is implemented

TABLE 1: Asphalt mastic gradation.

| Sieve size (mm) | 1.18 | 0.6 | 0.3 | 0.15 | 0.075 |
|-----------------|------|-----|-----|------|-------|
| Passing percent | 100 | 75 | 46 | 33 | 29 |

to ensure that the asphalt mastic in asphalt mastic samples is similar to that existing in asphalt concrete samples.

3.2. Numerical Tests. Figure 9 plots a diagram of the dynamic modulus numerical test. The same loading condition used in the laboratory tests is applied in the numerical simulations. A certain loading frequency equal to that used in the laboratory test is applied to the upper horizontal wall of the numerical sample in the y -direction to simulate the loading procedure, while the bottom horizontal wall used to support the numerical sample is fixed in all the directions.

To ensure the reliability of simulations, the parallel tests are implemented in numerical simulation just as experiment tests. In experimental parallel tests, the asphalt concrete samples usually have the same raw materials and material composition and the random material distribution. Accordingly, in numerical parallel tests, the numerical models have the same material parameters and material composition and the random microstructure distribution.

Moreover, it should be explained that the same series of parallel numerical samples are employed to simulate the dynamic modulus and phase angle of different types of numerical samples in this study. It is beneficial to compare the difference in the rheological behaviors in the case of using different mesoscopic viscoelastic contact models more clearly without the impact of mesoscopic structures (such as aggregate characteristics and void characteristics) and their distributions. In addition, the influences of the temperatures on the behaviors of asphalt concrete are represented indirectly via the difference in parameters calibrated at different temperatures, as shown in Tables 2–4.

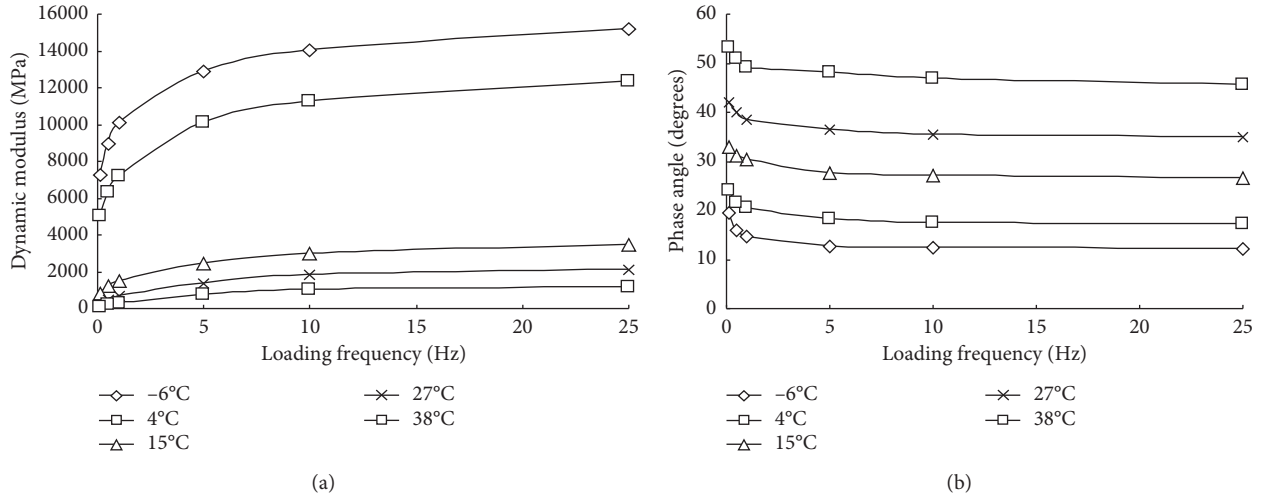


FIGURE 5: Testing results of the asphalt mastic.

TABLE 2: Parameters of the numerical samples using the B-model.

| T (°C) | Direction | k_0^B | k_1^B | η_1^B | k_2^B | η_2^B |
|----------|-----------|---------|---------|------------|---------|------------|
| -6 | Normal | 118.40 | 8.11 | 1.66 | 4.26 | 5.19 |
| | Shear | 307.84 | 2.71 | 0.55 | 1.42 | 1.73 |
| 4 | Normal | 118.40 | 6.29 | 2.19 | 3.88 | 5.33 |
| | Shear | 307.84 | 2.11 | 0.73 | 1.29 | 1.78 |
| 15 | Normal | 118.40 | 4.83 | 2.88 | 2.96 | 6.68 |
| | Shear | 307.84 | 1.61 | 0.96 | 0.99 | 2.23 |
| 27 | Normal | 118.40 | 2.76 | 3.27 | 1.77 | 7.12 |
| | Shear | 307.84 | 0.92 | 1.09 | 0.59 | 2.37 |
| 38 | Normal | 118.40 | 1.51 | 3.99 | 1.26 | 7.79 |
| | Shear | 307.84 | 0.50 | 1.33 | 0.42 | 2.60 |

TABLE 3: Parameters of the numerical samples using the M-model.

| T (°C) | Direction | k_0^M | k_1^M | η_1^M | k_2^M | η_2^M | k_3^M | η_3^M | k_4^M | η_4^M | k_5^M | η_5^M |
|----------|-----------|---------|---------|------------|---------|------------|---------|------------|---------|------------|---------|------------|
| -6 | Normal | 118.40 | 7.81 | 0.02 | 7.05 | 1.22 | 7.10 | 11.10 | 7.60 | 0.16 | 0.94 | 5.81 |
| | Shear | 307.84 | 2.79 | 0.01 | 2.16 | 0.41 | 2.54 | 3.70 | 2.71 | 0.05 | 0.34 | 1.93 |
| 4 | Normal | 118.40 | 4.56 | 0.02 | 3.31 | 2.10 | 3.17 | 1.26 | 6.16 | 0.08 | 0.62 | 1.66 |
| | Shear | 307.84 | 1.53 | 0.01 | 1.17 | 0.67 | 1.24 | 0.55 | 1.89 | 0.03 | 0.18 | 0.51 |
| 15 | Normal | 118.40 | 3.11 | 0.77 | 3.40 | 2.41 | 3.61 | 1.96 | 5.51 | 0.09 | 0.52 | 1.85 |
| | Shear | 307.84 | 1.04 | 0.26 | 1.13 | 0.80 | 1.21 | 0.65 | 1.84 | 0.03 | 0.18 | 0.62 |
| 27 | Normal | 118.40 | 1.96 | 1.11 | 5.57 | 0.98 | 4.88 | 9.64 | 4.78 | 0.14 | 0.65 | 7.21 |
| | Shear | 307.84 | 0.65 | 0.37 | 1.86 | 0.33 | 1.63 | 3.22 | 1.60 | 0.05 | 0.22 | 2.40 |
| 38 | Normal | 118.40 | 0.67 | 2.31 | 1.62 | 6.08 | 2.66 | 9.20 | 0.55 | 9.26 | 1.12 | 8.07 |
| | Shear | 307.84 | 0.22 | 0.77 | 0.54 | 2.03 | 0.89 | 3.07 | 0.18 | 3.09 | 0.37 | 4.36 |

TABLE 4: Parameters of the numerical samples using the K-model.

| T (°C) | Direction | k_0^K | k_1^K | η_1^K | k_2^K | η_2^K | k_3^K | η_3^K | k_4^K | η_4^K | k_5^K | η_5^K |
|----------|-----------|---------|---------|------------|---------|------------|---------|------------|---------|------------|---------|------------|
| -6 | Normal | 118.40 | 8.79 | 1.46 | 6.61 | 2.32 | 2.11 | 2.61 | 1.61 | 3.51 | 3.00 | 3.00 |
| | Shear | 307.84 | 2.93 | 0.48 | 2.21 | 0.77 | 0.71 | 0.87 | 0.55 | 1.17 | 1.00 | 1.00 |
| 4 | Normal | 118.40 | 6.61 | 1.99 | 4.51 | 3.11 | 1.40 | 2.62 | 4.38 | 3.05 | 6.66 | 1.12 |
| | Shear | 307.84 | 2.21 | 0.66 | 1.50 | 1.04 | 0.47 | 0.87 | 1.46 | 1.01 | 2.22 | 0.37 |
| 15 | Normal | 118.40 | 4.97 | 2.67 | 3.66 | 3.59 | 3.50 | 6.11 | 3.19 | 1.82 | 1.82 | 5.11 |
| | Shear | 307.84 | 1.66 | 0.89 | 1.22 | 1.19 | 1.17 | 2.04 | 1.06 | 0.61 | 0.61 | 1.71 |
| 27 | Normal | 118.40 | 2.79 | 3.18 | 3.07 | 4.60 | 2.03 | 5.91 | 2.46 | 6.16 | 3.89 | 4.60 |
| | Shear | 307.84 | 0.93 | 1.06 | 1.02 | 1.53 | 0.68 | 1.97 | 0.82 | 2.06 | 1.30 | 1.53 |
| 38 | Normal | 118.40 | 1.51 | 3.82 | 2.62 | 3.96 | 3.86 | 5.46 | 2.67 | 5.68 | 3.56 | 4.13 |
| | Shear | 307.84 | 0.50 | 1.27 | 0.87 | 1.32 | 1.29 | 1.82 | 0.89 | 1.89 | 1.19 | 1.38 |

TABLE 5: Material composition of asphalt concrete.

| Aggregate gradation | | Asphalt binder content | | Air void | | Asphalt mastic content | |
|---------------------|----------|------------------------|------------|----------|------------|------------------------|------------|
| Sieve size (mm) | Mass (%) | Mass (%) | Volume (%) | Mass (%) | Volume (%) | Mass (%) | Volume (%) |
| 16 | 100 | | | | | | |
| 13.2 | 87 | | | | | | |
| 9.5 | 70 | | | | | | |
| 4.75 | 40 | | | | | | |
| 2.36 | 28 | 4.5 | 10.9 | 0 | 4 | 27.4 | 31.8 |
| 1.18 | 24 | | | | | | |
| 0.6 | 18 | | | | | | |
| 0.3 | 11 | | | | | | |
| 0.15 | 8 | | | | | | |
| 0.075 | 7 | | | | | | |

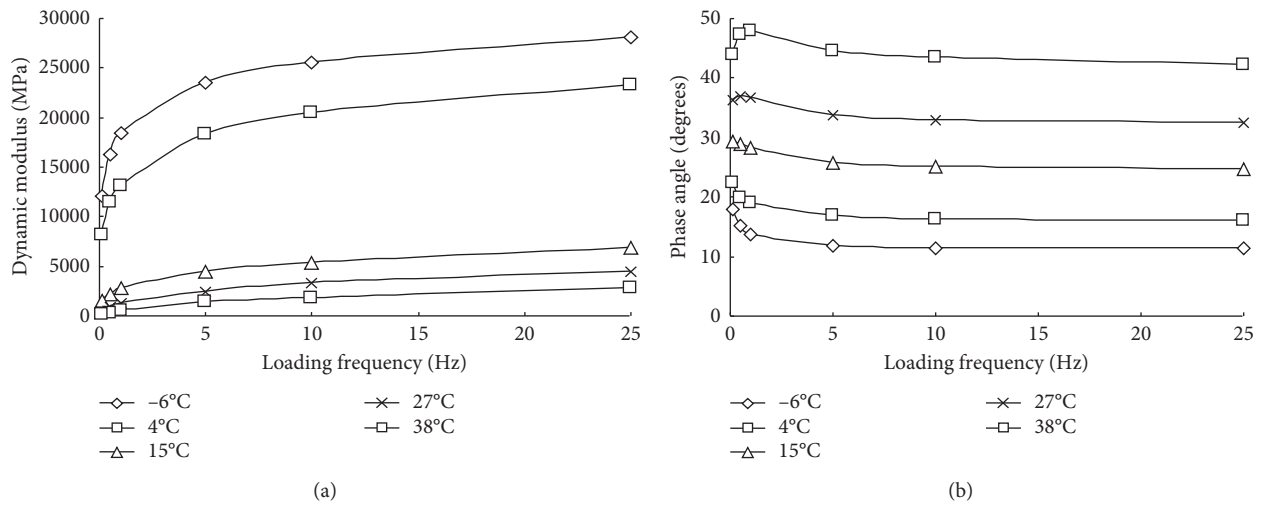


FIGURE 6: Testing results of asphalt concrete.



FIGURE 7: Schematic of the dynamic modulus test.

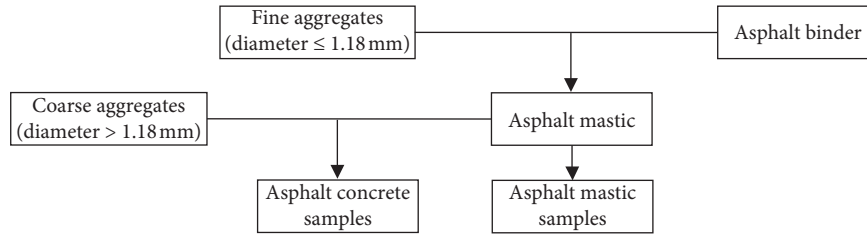


FIGURE 8: Preparation process of asphalt concrete samples and asphalt mastic samples.

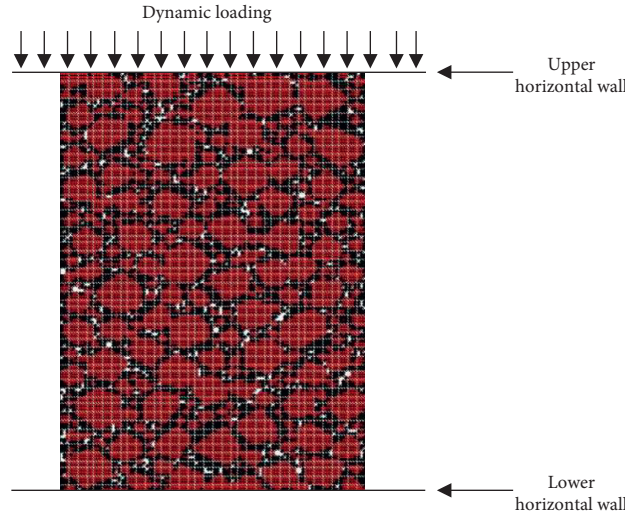


FIGURE 9: Dynamic modulus numerical test.

4. Results and Discussion

To evaluate the simulation precision, the relative errors between simulation results and laboratory data are calculated using the following equation:

$$\text{Error}_{|E|} = \left| \frac{|E|_{\text{DEM}} - |E|_{\text{Lab}}}{|E|_{\text{Lab}}} \right|, \quad (1)$$

$$\text{Error}_{\theta} = \left| \frac{\theta_{\text{DEM}} - \theta_{\text{Lab}}}{\theta_{\text{Lab}}} \right|,$$

where $\text{Error}_{|E|}$ and Error_{θ} are the error of dynamic modulus and phase angle, $|E|_{\text{DEM}}$ and $|E|_{\text{Lab}}$ are the simulation results and laboratory data of dynamic modulus, and θ_{DEM} and θ_{Lab} are the simulation results and laboratory data of phase angle.

Moreover, the curves in the following are given in the linear-log scales to plot the results clearly at low frequencies.

4.1. Dynamic Modulus. Figures 10 and 11 plot the data comparison and error analysis of dynamic modulus.

As shown in Figures 10 and 11, the following observations can be made:

- (1) At the low temperatures (-6°C and 4°C), the numerical samples using the M-model provide the best simulation precision. The relative errors in the case of using the M-model at different frequencies are on

average 4.72% and 4.74% at -6°C and 4°C , respectively, while those in the case of using the B-model (K-model) are on average 8.05% (8.02%) and 6.93% (6.74%) at -6°C and 4°C . The maximum errors in the case of using the M-model at different frequencies are 6.69% and 7.15% at -6°C and 4°C , respectively, while those in the case of using the B-model (K-model) are 10.78% (10.09%) and 14.72% (7.38%) at -6°C and 4°C . In addition, the effects of temperatures on the simulation precision in the case of using the M-model are not obvious.

- (2) With the rise of temperature, the numerical samples using the K-model gradually show the improved simulation precisions. The relative errors in the case of using the K-model at different frequencies are only on average 3.50% and 2.97% at 27°C and 38°C , respectively, while those in the case of using the B-model (M-model) are on average 6.41% (5.02%) and 6.84% (3.74%) at 27°C and 38°C . The maximum errors in the case of using the K-model at different frequencies are 6.41% and 5.17% at 27°C and 38°C , respectively, while those in the case of using the B-model and M-model are on average 10.18% (7.42%) and 10.93% (5.33%) at 27°C and 38°C .
- (3) The effects of frequency on the simulation precision are very limited in the case of using the M-model and K-model. The relative errors in the case of using the

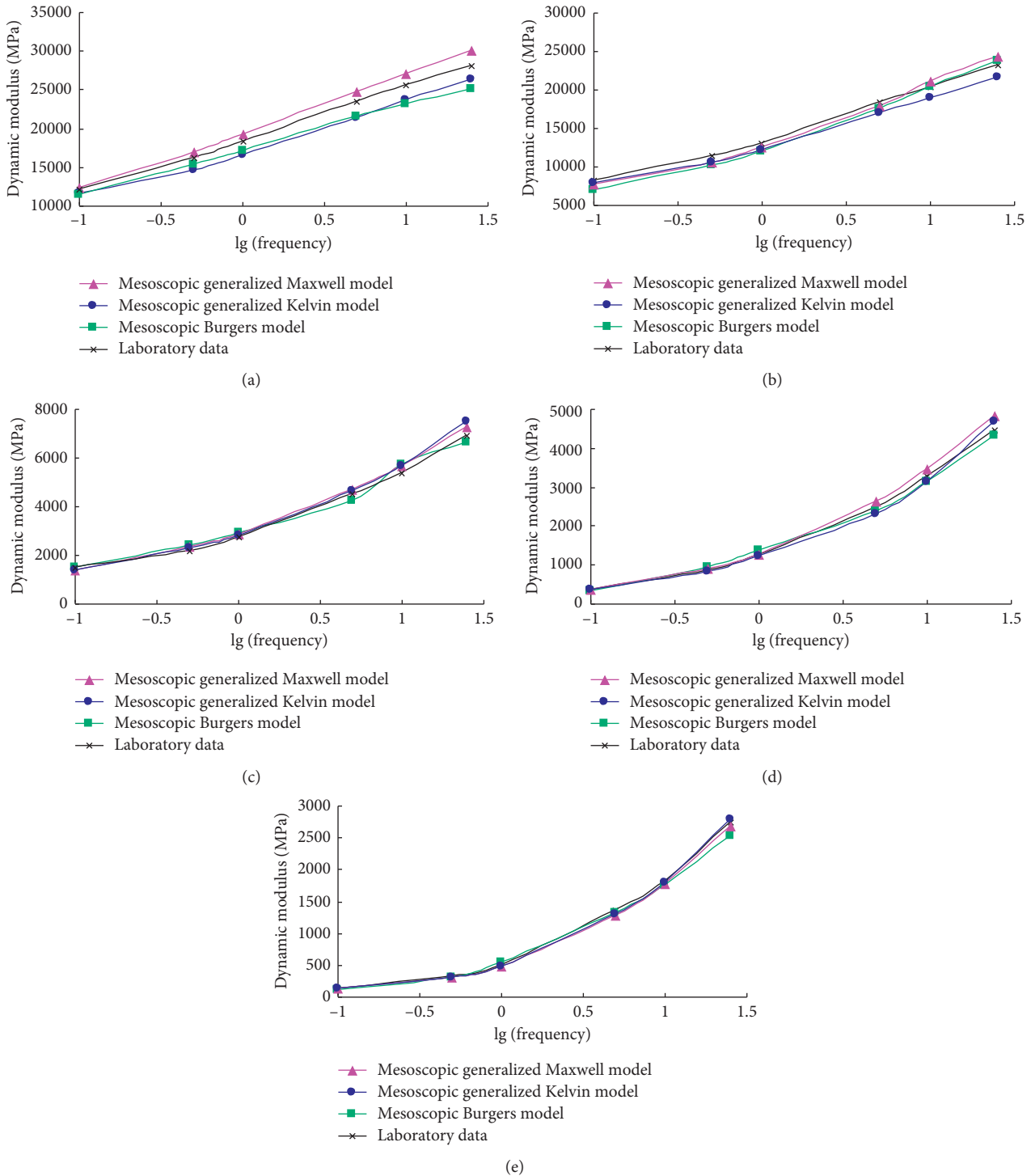


FIGURE 10: Laboratory data and simulation results of dynamic modulus. (a) -6°C . (b) 4°C . (c) 16°C . (d) 27°C . (e) 38°C .

M-model (K-model) at different temperatures are on average 5.27% (4.16%), 5.23% (5.39%), 3.95% (4.98%), 4.77% (6.45%), 4.25% (5.19%), and 5.68% (5.11%) at 0.1 Hz, 0.5 Hz, 1 Hz, 5 Hz, 10 Hz, and 25 Hz, respectively.

(4) Although the simulation precision in the case of using the B-model is lower than that of the other

two contact models, the relative error at different test conditions (frequency and temperature) still reaches an acceptable level (on average 6.79%). The relative errors in the case of using the M-model and K-model at different test conditions are on average 4.76% and 5.31%, respectively. The difference is not significant.

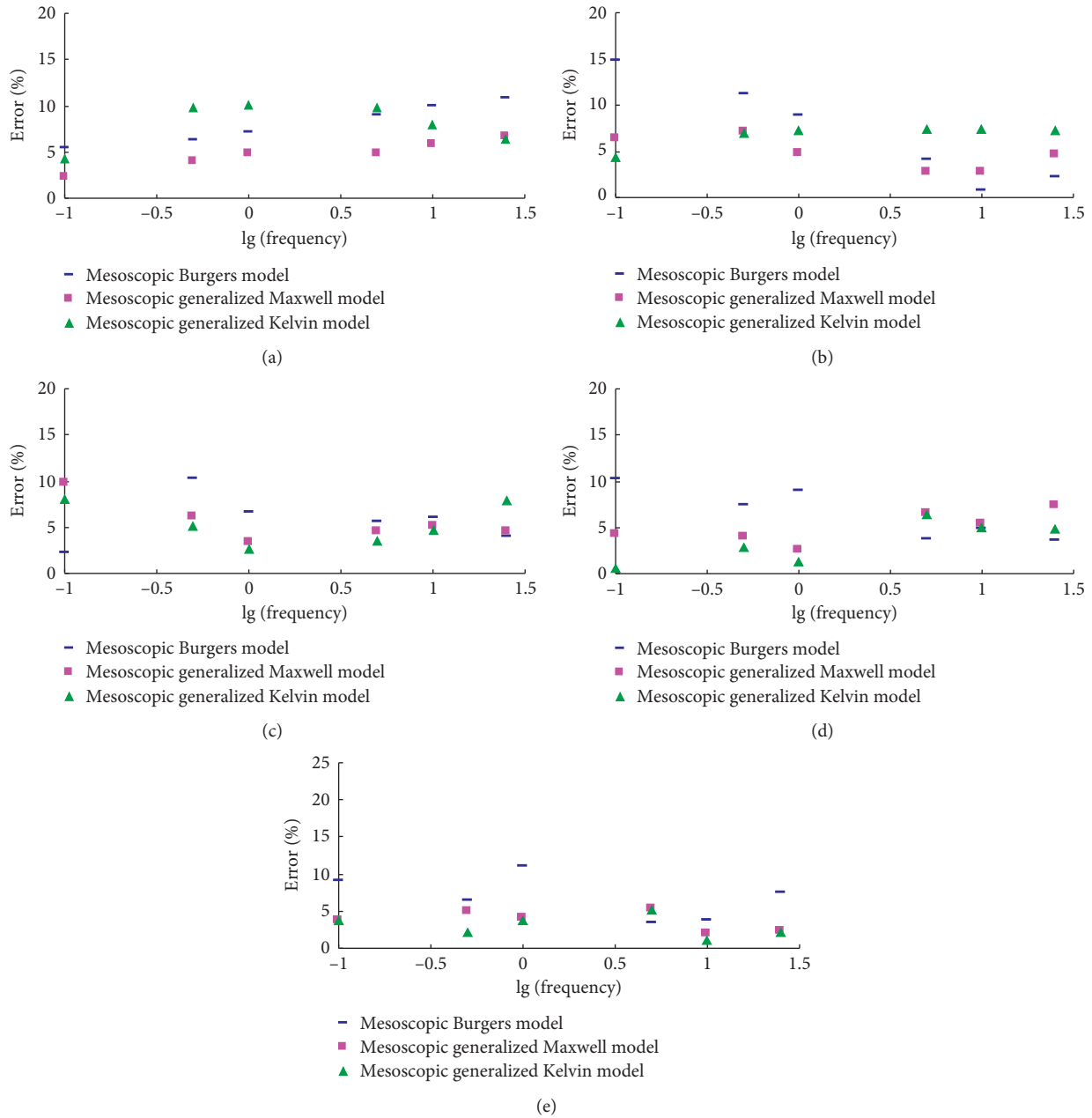


FIGURE 11: Errors of dynamic modulus. (a) -6°C . (b) 4°C . (c) 16°C . (d) 27°C . (e) 38°C .

4.2. Phase Angle. Figures 12 and 13 plot the data comparison and error analysis of phase angle.

As shown in Figures 12 and 13, the following observations can be made:

- (1) Similarly to the dynamic modulus, the numerical samples using the M-model also provide the best simulation precision for the phase angle at the low temperature (-6°C and 4°C). The relative errors in the case of using the M-model at different frequencies are on average 2.72% and 4.74% at -6°C and 4°C , respectively, while those in the case of using the B-model (K-model) are on average 18.43% (6.62%) and 16.19% (5.16%) at -6°C and 4°C . The maximum

errors in the case of using the M-model at different frequencies are 5.93% and 6.91% at -6°C and 4°C , respectively, while those in the case of using the B-model (K-model) are 73.93% (12.31%) and 58.69% (9.19%) at -6°C and 4°C . It can be found that the advantage of the M-model in evaluating the phase angle is more obvious than when evaluating the dynamic modulus. In addition, the effects of temperatures on the simulation precision of phase angle are also not obvious in the case of using the M-model.

- (2) The simulation precision of phase angle gradually improves with the increasing temperature. The relative errors in the case of using different numerical samples

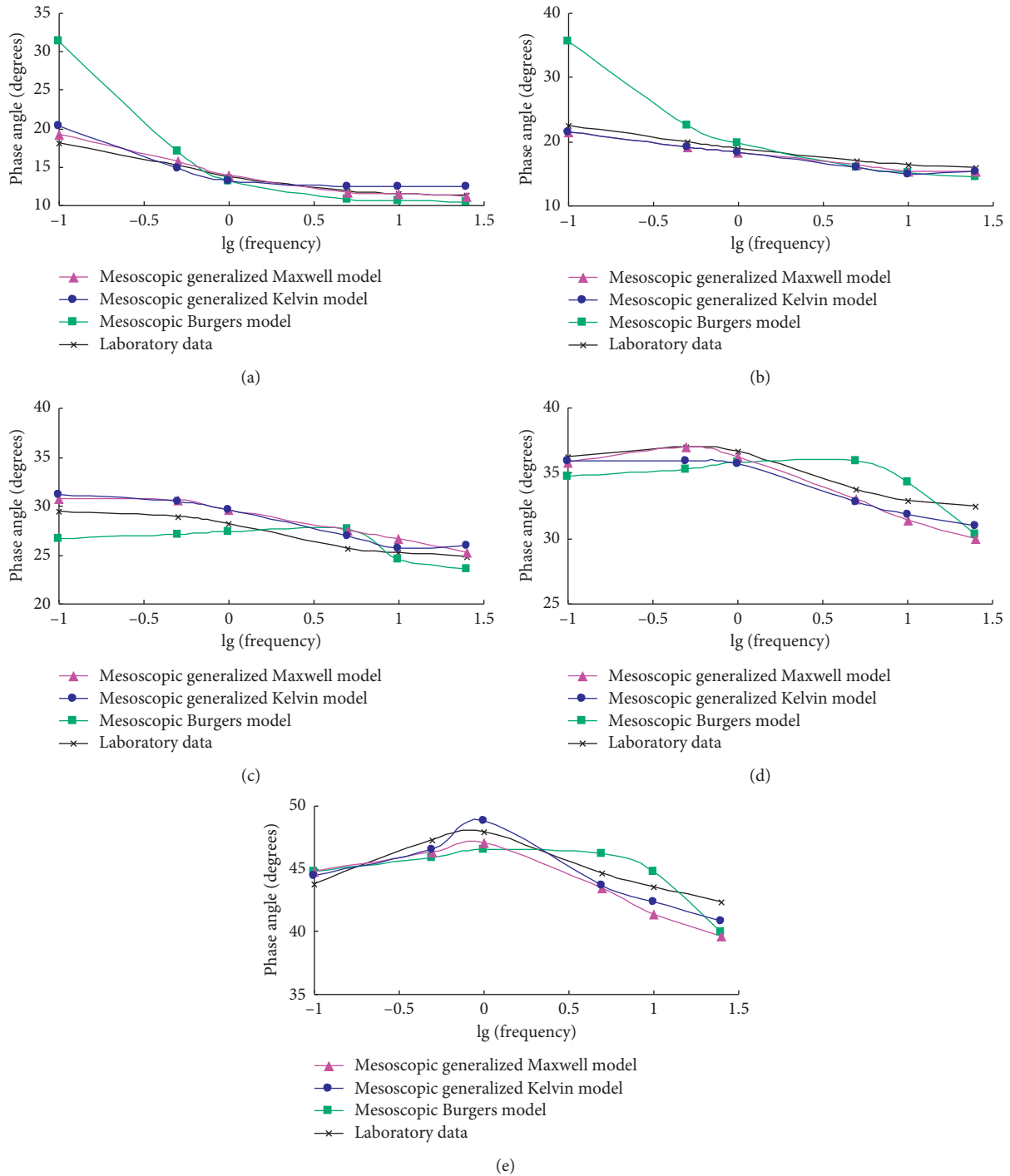


FIGURE 12: Laboratory data and simulation results of phase angle. (a) -6°C . (b) 4°C . (c) 16°C . (d) 27°C . (e) 38°C .

at different frequencies are on average 9.25%, 8.69%, 5.05%, 3.51%, and 2.49% at -6°C , 4°C , 16°C , 27°C , and 38°C , respectively. The maximum errors in the case of using different numerical samples are on average 30.72%, 24.93%, 7.56%, 6.23%, and 5.14% at -6°C , 4°C , 16°C , 27°C , and 38°C , respectively. In fact, when the temperature exceeds 15°C , the difference in the simulation precision in the case of using the three contact models is not significant. However, the numerical

samples using the K-model still show a certain advantage. The relative errors in the case of using the K-model at different frequencies are on average 4.63%, 2.93%, and 2.20% at 15°C , 27°C , and 38°C , respectively, while those in the case of using the B-model (M-model) are on average 5.60% (4.93%), 4.71% (2.88%), and 6.84% (3.31%) at 15°C , 27°C , and 38°C .

(3) The effects of frequency on the simulation precision are very limited in the case of using M-model and

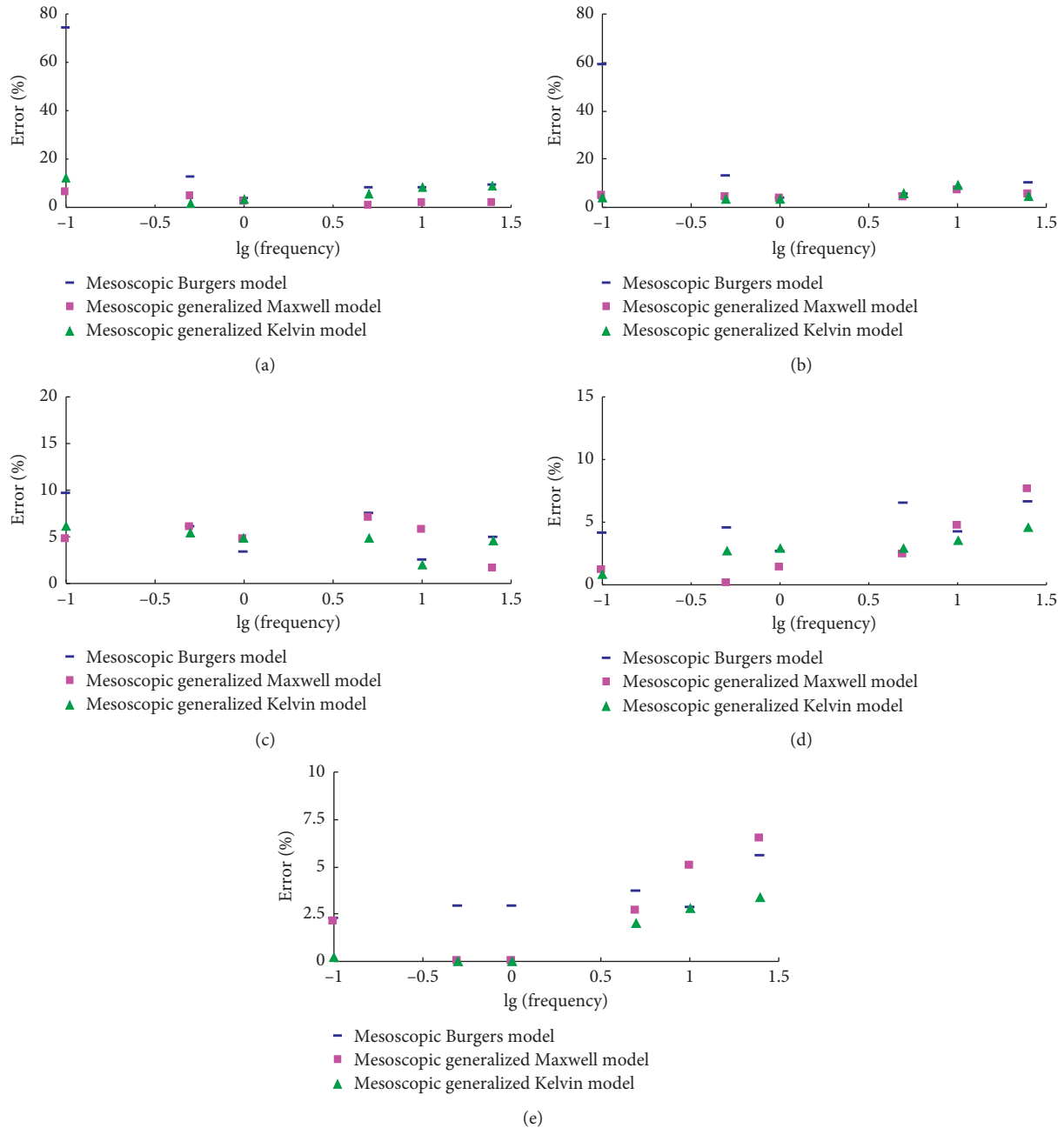


FIGURE 13: Errors of phase angle. (a) -6°C . (b) 4°C . (c) 16°C . (d) 27°C . (e) 38°C .

K-model. The relative errors in the case of using the M-model (K-model) at different temperatures are on average 3.71% (5.00%), 3.35% (3.02%), 2.67% (3.22%), 3.27% (4.26%), 4.75% (5.16%), and 4.50% (5.16%) at 0.1 Hz, 0.5 Hz, 1 Hz, 5 Hz, 10 Hz, and 25 Hz, respectively.

- (4) Different from the simulations of dynamic modulus, the precision of phase angle in the case of using the B-model is obviously lower than that of the other two contact models, particularly at low temperatures and frequencies. The average errors (maximum errors) at different frequencies are 19.03% (73.93%) and 16.19% (58.69%) at -6°C and 4°C . The maximum

errors and the secondary maximum errors all appear at the frequencies of 0.1 Hz and 0.5 Hz.

5. Concluding Remarks

In this study, the influence of mesoscopic viscoelastic contact models in the DEM on characterizing the rheological behavior of asphalt concrete is investigated based on the comparison between laboratory tests and the corresponding numerical tests via the rheological indexes of dynamic modulus and phase angle at different temperatures (-6°C , 4°C , 16°C , 27°C , and 38°C) and loading frequencies (0.1 Hz, 0.5 Hz, 1 Hz, 5 Hz, 10 Hz, and 25 Hz). The following observations can be made:

- (i) The difference in simulation precision in the case of using the three mesoscopic viscoelastic contact models at different temperatures is more significant than that at different frequencies.
- (ii) The difference in simulation precision of phase angle in the case of using the three mesoscopic viscoelastic contact models is more obvious than that of the dynamic modulus.
- (iii) The mesoscopic generalized Maxwell contact model provides the best simulation precision at low temperature. The absolute level of the simulation precision is little changed with the temperature and frequency.
- (iv) The mesoscopic generalized Kelvin contact model shows an improved simulation precision at high temperatures, and this advantage is more significant with the increased temperature. However, the frequency has less effect on the absolute value of the simulation precision.
- (v) The simulation precision of the mesoscopic Burgers contact model is obviously lower than that of the other two contact models, particularly when simulating the phase angle at low temperatures and frequencies. However, the simulation precision is acceptable when the temperature exceeds 15°C, particularly for the dynamic modulus. Considering the relatively simple mathematical structure, the mesoscopic Burgers contact model can also be used in the DEM simulations at medium and high temperatures.

Data Availability

The data used to support the findings of this study are included within the article.

Conflicts of Interest

The authors declare that they have no conflicts of interest.

Acknowledgments

This study was sponsored in part by the National Natural Science Foundation of China under grant 51808326, by the Natural Science Foundation of Zhejiang Province under grant LQY19E080002, and by the Doctoral Research Foundation of Hubei University of Arts and Science under grant 2059084, to which the authors are very grateful.

References

- [1] J. Li, G. Liu, T. Yang, J. Zhou, and Y. Zhao, "Research on relationships among different distress types of asphalt pavements with semi-rigid bases in China using association rule mining: a statistical point of view," *Advances in Civil Engineering*, vol. 2019, Article ID 5369532, 15 pages, 2019.
- [2] Y.-R. Kim and D. N. Little, "Linear viscoelastic analysis of asphalt mastics," *Journal of Materials in Civil Engineering*, vol. 16, no. 2, pp. 122–132, 2004.
- [3] Y. Tan and M. Guo, "Study on the phase behavior of asphalt mastic," *Construction and Building Materials*, vol. 47, pp. 311–317, 2013.
- [4] J. Li, M. Shang, G. Liu et al., "Two-step improvements of volumetric design method based on multi-point supported skeleton for asphalt mixtures," *Construction and Building Materials*, vol. 217, pp. 456–472, 2019.
- [5] J. Li, M. Shang, Y. Pan et al., "Laboratory improvement and field assessment of volumetric design method based on multi-point supported skeleton for asphalt mixtures (V-S method)," *Construction and Building Materials*, vol. 224, pp. 962–979, 2019.
- [6] P. A. Cundall, "A computer model for simulating progressive large-scale movements in blocky rock systems," in *Proceedings of the International Symposium on Rock Fracture Mechanics*, Nancy, France, October 1971.
- [7] P. A. Cundall and O. D. L. Strack, "A discrete numerical model for granular assemblies," *Géotechnique*, vol. 29, no. 1, pp. 47–65, 1979.
- [8] Z. Qin, H. Fu, and X. Chen, "A study on altered granite meso-damage mechanisms due to water invasion-water loss cycles," *Environmental Earth Sciences*, vol. 78, no. 14, p. 428, 2019.
- [9] Z. You and Q. Dai, "Review of advances in micromechanical modeling of aggregate-aggregate interactions in asphalt mixtures," *Canadian Journal of Civil Engineering*, vol. 34, no. 2, pp. 239–252, 2007.
- [10] H. Kim, M. P. Wagoner, and W. G. Buttlar, "Simulation of fracture behavior in asphalt concrete using a heterogeneous cohesive zone discrete element model," *Journal of Materials in Civil Engineering*, vol. 20, no. 8, pp. 552–563, 2008.
- [11] H. Kim and W. G. Buttlar, "Multi-scale fracture modeling of asphalt composite structures," *Composites Science and Technology*, vol. 69, no. 15–16, pp. 2716–2723, 2009.
- [12] H. Kim, M. P. Wagoner, and W. G. Buttlar, "Numerical fracture analysis on the specimen size dependency of asphalt concrete using a cohesive softening model," *Construction and Building Materials*, vol. 23, no. 5, pp. 2112–2120, 2009.
- [13] E. Mahmoud, E. Masad, and S. Nazarian, "Discrete element analysis of the influences of aggregate properties and internal structure on fracture in asphalt mixtures," *Journal of Materials in Civil Engineering*, vol. 22, no. 1, pp. 10–20, 2010.
- [14] Z. Qian, J. Wang, L. Chen, and L. Wang, "Three-dimensional discrete element modeling of crack development in epoxy asphalt concrete," *Journal of Testing and Evaluation*, vol. 43, no. 2, pp. 295–307, 2015.
- [15] X. Yang, Q. Dai, Z. You, and Z. Wang, "Integrated experimental-numerical approach for estimating asphalt mixture induction healing level through discrete element modeling of a single-edge notched beam test," *Journal of Materials in Civil Engineering*, vol. 27, no. 9, Article ID 04014259, 2015.
- [16] J. Chen, T. Pan, and X. Huang, "Discrete element modeling of asphalt concrete cracking using a user-defined three-dimensional micromechanical approach," *Journal of Wuhan University of Technology-Materials Science Edition*, vol. 26, no. 6, pp. 1215–1221, 2011.
- [17] J. Chen, T. Pan, and X. Huang, "Numerical investigation into the stiffness anisotropy of asphalt concrete from a micro-structural perspective," *Construction and Building Materials*, vol. 25, no. 7, pp. 3059–3065, 2011.
- [18] H. Feng, M. Pettinari, and H. Stang, "Study of normal and shear material properties for viscoelastic model of asphalt mixture by discrete element method," *Construction and Building Materials*, vol. 98, pp. 366–375, 2015.

- [19] M. J. Khattak and C. Roussel, "Micromechanical modeling of hot-mix asphalt mixtures by imaging and discrete element methods," *Transportation Research Record: Journal of the Transportation Research Board*, vol. 2127, no. 1, pp. 98–106, 2009.
- [20] H. Kim, M. P. Wagoner, and W. G. Buttlar, "Rate-dependent fracture modeling of asphalt concrete using the discrete element method," *Canadian Journal of Civil Engineering*, vol. 36, no. 2, pp. 320–330, 2009.
- [21] X. Li, X. Lv, X. Liu, and J. Ye, "Discrete element analysis of indirect tensile fatigue test of asphalt mixture," *Applied Sciences*, vol. 9, no. 2, p. 327, 2019.
- [22] Y. Liu and Z. You, "Visualization and simulation of asphalt concrete with randomly generated three-dimensional models," *Journal of Computing in Civil Engineering*, vol. 23, no. 6, pp. 340–347, 2009.
- [23] Y. Liu and Z. You, "Accelerated discrete-element modeling of asphalt-based materials with the frequency-temperature superposition principle," *Journal of Engineering Mechanics*, vol. 137, no. 5, pp. 355–365, 2011.
- [24] Y. Liu and Z. You, "Discrete-element modeling: impacts of aggregate sphericity, orientation, and angularity on creep stiffness of idealized asphalt mixtures," *Journal of Engineering Mechanics*, vol. 137, no. 4, pp. 294–303, 2011.
- [25] Y. Liu, Z. You, and Y. Zhao, "Three-dimensional discrete element modeling of asphalt concrete: size effects of elements," *Construction and Building Materials*, vol. 37, pp. 775–782, 2012.
- [26] T. Ma, H. Wang, D. Zhang, and Y. Zhang, "Heterogeneity effect of mechanical property on creep behavior of asphalt mixture based on micromechanical modeling and virtual creep test," *Mechanics of Materials*, vol. 104, pp. 49–59, 2017.
- [27] E. Olsson, D. Jelagin, and M. N. Partl, "New discrete element framework for modelling asphalt compaction," *Road Materials and Pavement Design*, vol. 20, no. sup2, pp. s604–s616, 2019.
- [28] Y. Peng and J. Bao, "Micromechanical analysis of asphalt-mixture shear strength using the three-dimensional discrete element method," *Journal of Materials in Civil Engineering*, vol. 30, no. 11, Article ID 04018302, 2018.
- [29] Z. You, S. Adhikari, and Q. Dai, "Air void effect on an idealised asphalt mixture using two-dimensional and three-dimensional discrete element modelling approach," *International Journal of Pavement Engineering*, vol. 11, no. 5, pp. 381–391, 2010.
- [30] Z. You, Y. Liu, and Q. Dai, "Three-dimensional microstructural-based discrete element viscoelastic modeling of creep compliance tests for asphalt mixtures," *Journal of Materials in Civil Engineering*, vol. 23, no. 1, pp. 79–87, 2011.
- [31] H. M. Zelelew and A. T. Papagiannakis, "Micromechanical modeling of asphalt concrete uniaxial creep using the discrete element method," *Road Materials and Pavement Design*, vol. 11, no. 3, pp. 613–632, 2011.
- [32] D. Zhang, X. Huang, and Y. Zhao, "Algorithms for generating three-dimensional aggregates and asphalt mixture samples by the discrete-element method," *Journal of Computing in Civil Engineering*, vol. 27, no. 2, pp. 111–117, 2013.
- [33] D. Zhang, S. Hou, J. Bian, and L. He, "Investigation of the micro-cracking behavior of asphalt mixtures in the indirect tensile test," *Engineering Fracture Mechanics*, vol. 163, pp. 416–425, 2016.
- [34] Y. Zhang, T. Ma, M. Ling, D. Zhang, and X. Huang, "Predicting dynamic shear modulus of asphalt mastics using discretized-element simulation and reinforcement mechanisms," *Journal of Materials in Civil Engineering*, vol. 31, no. 8, Article ID 04019163, 2019.
- [35] J. Ren and L. Sun, "Generalized Maxwell viscoelastic contact model-based discrete element method for characterizing low-temperature properties of asphalt concrete," *Journal of Materials in Civil Engineering*, vol. 28, no. 2, Article ID 04015122, 2016.
- [36] J. Ren and L. Sun, "Characterizing air void effect on fracture of asphalt concrete at low-temperature using discrete element method," *Engineering Fracture Mechanics*, vol. 170, pp. 23–43, 2017.
- [37] L. Sun, J. Ren, and S. Zhang, "Fracture characteristics of asphalt concrete in mixed-loading mode at low-temperature based on discrete-element method," *Journal of Materials in Civil Engineering*, vol. 30, no. 12, Article ID 04018321, 2018.
- [38] Y. Xu, Y. Jiang, J. Xue, and J. Ren, "Investigating the effect of aggregate characteristics on the macroscopic and microscopic fracture mechanisms of asphalt concrete at low-temperature," *Materials*, vol. 12, no. 17, p. 2675, 2019.
- [39] Y. Shimizu, H. Ito, T. Sadakane, and T. Yamaguchi, "Multi-visco-elastic contact model in discrete element method-application to margarine's process engineering," *Nihon Reorji Gakkaishi*, vol. 40, no. 5, pp. 257–266, 2013.
- [40] A. Jin, K. Wang, X. Zhang, X. Meng, and Z. Yang, "A generalized Kelvin model based on the particle flow code and its application," *Rock and Soil Mechanics*, vol. 36, no. 9, pp. 2695–2701, 2015, in Chinese.
- [41] J. Wang, S.-C. Li, L.-P. Li, P. Lin, Z.-H. Xu, and C.-L. Gao, "Attribute recognition model for risk assessment of water inrush," *Bulletin of Engineering Geology and the Environment*, vol. 78, no. 2, pp. 1057–1071, 2019.